remote sensing

Article

An Advanced Spatiotemporal Fusion Model for Suspended Particulate Matter Monitoring in an Intermontane Lake

Fei Zhang [1,2,*,†], Pan Duan [2,3,†], Chi Yung Jim [4], Verner Carl Johnson [5], Changjiang Liu [2,6], Ngai Weng Chan [7], Mou Leong Tan [7], Hsiang-Te Kung [8], Jingchao Shi [8] and Weiwei Wang [2]

1 College of Geography and Environmental Sciences, Zhejiang Normal University, Jinhua 321004, China
2 College of Geography and Remote Sensing Sciences, Xinjiang University, Urumqi 830017, China
3 College of Hydrology and Water Resources, Hohai University, Nanjing 210024, China
4 Department of Social Sciences, Education University of Hong Kong, Lo Ping Road, Tai Po, Hong Kong 999077, China
5 Department of Physical and Environmental Sciences, Colorado Mesa University, Grand Junction, CO 81501, USA
6 Xinjiang Institute of Technology, Aksu 843000, China
7 GeoInformatic Unit, Geography Section, School of Humanities, Universiti Sains Malaysia, Penang 11800, Malaysia
8 Departments of Earth Sciences, The University of Memphis, Memphis, TN 38152, USA
* Correspondence: zhangfei3s@163.com or zhangfei3s@xju.edu.cn
† These authors contributed equally to this work.

Abstract: Ebinur Lake is the largest brackish-water lake in Xinjiang, China. Strong winds constantly have an impact on this shallow water body, causing high variability in turbidity of water. Therefore, it is crucial to continuously monitor suspended particulate matter (SPM) for water quality management. This research aims to develop an advanced spatiotemporal fusion model based on the inversion technique that enables time-continuous and detailed monitoring of SPM over an intermontane lake. The findings shows that: (1) the enhanced spatial and temporal adaptive reflectance fusion model (ESTARFM) fusion in blue, green, red, and near infrared (NIR) bands was better than the flexible spatiotemporal data fusion (FSDAF) model in extracting SPM information; (2) the inversion model constructed by random forest (RF) outperformed the support vector machine (SVM) and partial least squares (PLS) algorithms; and (3) the SPM concentrations acquired from the fused images of Landsat 8 OLI and ESTARFM matched with the actual data of Ebinur Lake based on the visual perspective and accuracy assessment.

Keywords: Ebinur Lake; suspended particulate matter (SPM); water quality monitoring; enhanced spatial and temporal adaptive reflectance fusion model (ESTARFM)

check for updates

Citation: Zhang, F.; Duan, P.; Jim, C.Y.; Johnson, V.C.; Liu, C.; Chan, N.W.; Tan, M.L.; Kung, H.-T.; Shi, J.; Wang, W. An Advanced Spatiotemporal Fusion Model for Suspended Particulate Matter Monitoring in an Intermontane Lake. *Remote Sens.* **2023**, *15*, 1204. https://doi.org/10.3390/rs15051204

Academic Editor: Hatim Sharif

Received: 28 January 2023
Revised: 19 February 2023
Accepted: 20 February 2023
Published: 22 February 2023

1. Introduction

Inland lakes provide an important freshwater supply for agricultural activities and domestic water usage [1]. Especially in arid regions, as a primary water supply, lakes deserve thorough study to comprehend water quality variables and processes to facilitating sustainable water usage [2,3]. Suspended particulate matter (SPM) is one of the key indicators for assessing a lake's water quality [4]. SPM influences water transparency and turbidity, which serves as the carrier of oxygen, carbon, heavy metals, and nutrient substances [5,6]. Therefore, it is crucial that SPM concentrations be regularly monitored for effective lake management.

With the rapid development in water color remote sensing technologies, SPM concentrations and dynamic processes can be easily and effectively captured [7]. Spectral data from satellite sensors are commonly applied to reflect the water's optical properties indirectly using inversion techniques that were developed based on the concentration of SPM components in water bodies [8]. At present, empirical, analytical, and semi-empirical/semi-analytical are three major approaches of SPM satellite-based extraction [9]. The statistical relationship between the spectral data and the observed SPM concentration serves as the foundation for the empirical model development [10]. Generally, a regression model is constructed by selecting a single band or different bands combination [11]. The analytical method has high inversion accuracy and theoretical generality. However, it requires more sophisticated and expensive optical instrumentation to measure a water body's intrinsic optical parameters, which restricts its practical applications [12]. Various semi-empirical/semi-analytical methods such as the quasi-analytical algorithm (QAA) and water color simulator (WASI) can better tackle the complex relationships between remote sensing reflectance and water color parameter concentration [13]. In general, machine-learning techniques such as neural network, support vector machine (SVM) and random forest (RF) are included in semi-empirical methods [14]. The machine-learning method is more time and computationally effective. In contrast to SVM and RF, which are better suited for small samples, a neural network needs a large number of training samples [15]. Many studies have proven that RF is better than SVM in dealing with noise and outliers [16]. RF is also more amenable to interpretation and can provide solutions to the inversion problems [17]. Hence, this study has adopted RF to build the SPM concentration inversion model.

The acquisition of remote sensing data has been greatly improved. However, obtaining remote sensing data with high spatial and temporal resolution is still difficult [18]. At present, many spatiotemporal fusion models have been developed to enhance data quality and resolve the problem of missing remote sensing data [19]. Basically, these models are divided into four categories: transformation, filtering, unmixing, and dictionary learning [20]. The transformation model uses principal component analysis and wavelet transformation [21]. The filtering method predicts high-resolution images by introducing neighborhood information [22], including STARFM (spatial and temporal adaptive reflectance fusion model) [23], ESTARFM (enhanced spatial and temporal adaptive reflectance fusion model) [24], and STNLFFM (spatial and temporal non-local filter-based fusion model) [25]. The unmixing methods are USTARFM (unmixing-based STARFM) [26] and FSDAF (flexible spatiotemporal data fusion) [27]. The most representative sparse representation is based on the spatiotemporal reflectance fusion model (SPSTFM) [28]. Two major applications of spatiotemporal fusion models are land surface dynamic monitoring and land cover classification [29]. Some researchers have utilized ESTARFM to examine the water quality and area changes of freshwater lakes [30]. Therefore, ESTARFM was selected for the lake image fusion of Ebinur Lake in this paper.

To date, most studies have focused on inland lakes, while shallow saline lakes have received very little attention. Hence, the objectives of this study are to: (1) establish an SPM inversion model, focusing on the main characteristics of a shallow brackish lake with highly turbid water; (2) invert SPM using ESTARFM fusion images; and (3) assess the applicability of the developed spatiotemporal fusion model in SPM inversion for intermontane lakes. The model can be applied in other intermontane lakes to assist relevant scientists and local authorities to better characterize the spatiotemporal patterns of SPM. This study will act as a research basis for others' water quality parameters for inversion methods and water resources management.

2. Materials

2.1. Study Area

Ebinur Lake is located in the inland intermontane Ebinur Lake Basin in the northwest part of Xinjiang (44°05′~45°08′N, 82°35′~83°16′E) (Figure 1), surrounded by mountains in the north, west, and south of the basin. This arid landscape is located in the interior heart of Eurasia, is distant from the sea, and has irregular and erratic precipitation, high potential evapotranspiration, and a lot of solar radiation and heat. Subsumed under a typical continental climate, Ebinur Lake has an average temperature of 6.6~7.8 °C and annual precipitation of merely 116.0~169.2 mm. The northwest of the basin is renowned for a mountain wind gap known as the Alashan Pass. The annual wind (≥17.2 m/s) days amount to 164 d, and the maximum wind speed can reach 55.0 m/s. The average depth for the lake body is 1.4 m, the surface water density is 1.079 g/cm^3, the pH is 8.49, and the salinity is 112.4 g/L. The lake surface area fluctuates considerably throughout the year, and the water tends to remain highly turbid [31].

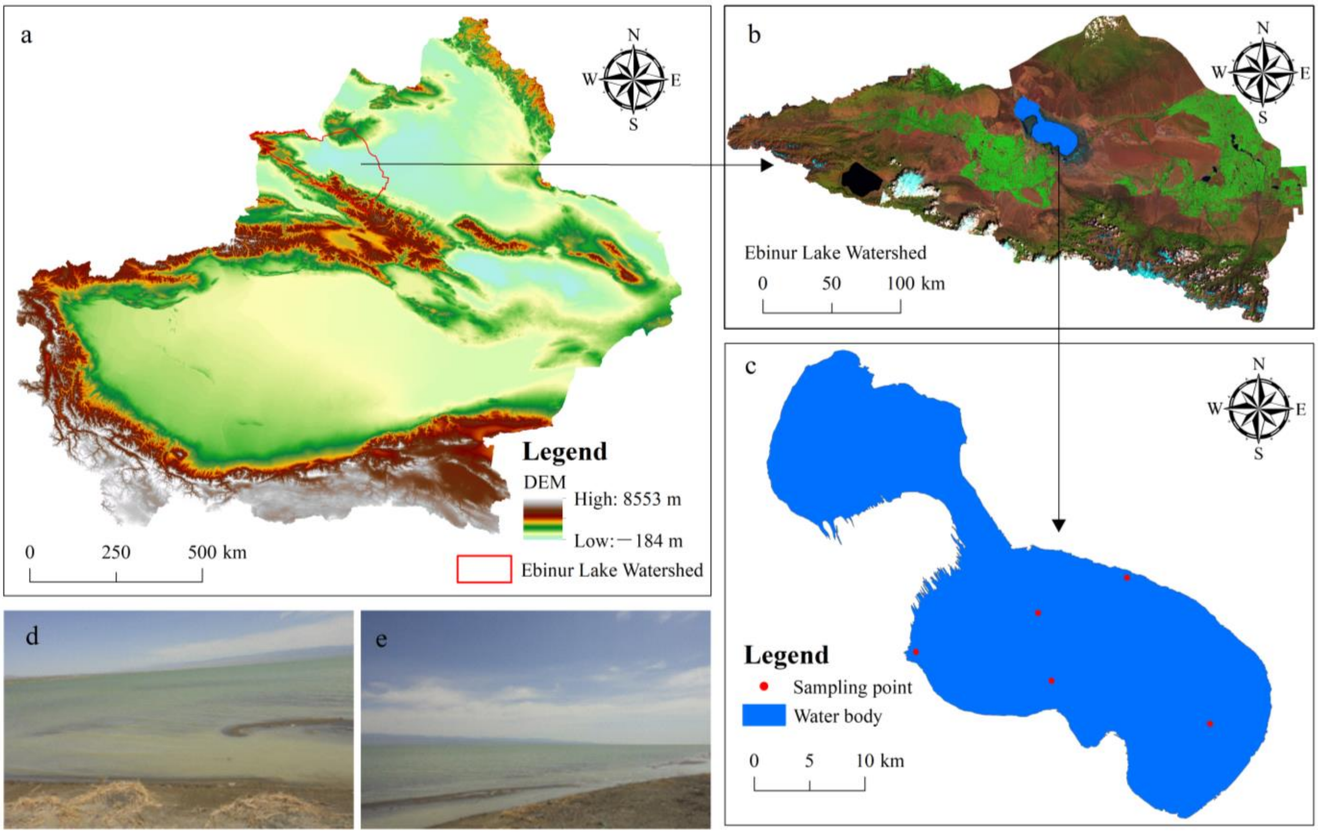

Figure 1. Location of study area: (**a**) The location and general relief of the Ebinur Lake Watershed in northwest Xinjiang, China; (**b**) The location of Ebinur Lake at the center of the Ebinur Lake Watershed; (**c**) Ebinur Lake with the locations of five sampling points; and (**d**,**e**) Ground photographs of Ebinur Lake and its arid landscape environs taken in May 2017.

2.2. Data Acquisition and Processing

Observed SPM data from five monitoring sites well distributed across the Ebinur Lake were collected in May, June, September, and October 2017 (Figure 1c). The SPM concentration collection and measurement were completed according to the standard GB11901-89 (1989) [32]. Table 1 lists the statistical characteristics of the collected SPM samples. The matching time between observed SPM and satellite images should be within the time window >±7 days [33], so a total of 42 samples, as shown in Figure 2, have been effectively matched and can be used for the next analysis.

Table 1. Statistical characteristics of SPM samples.

	Max (mg/L)	Min (mg/L)	Mean (mg/L)	Std (mg/L)
SPM (n = 42)	8350.00	18.50	1395.32	2376.33

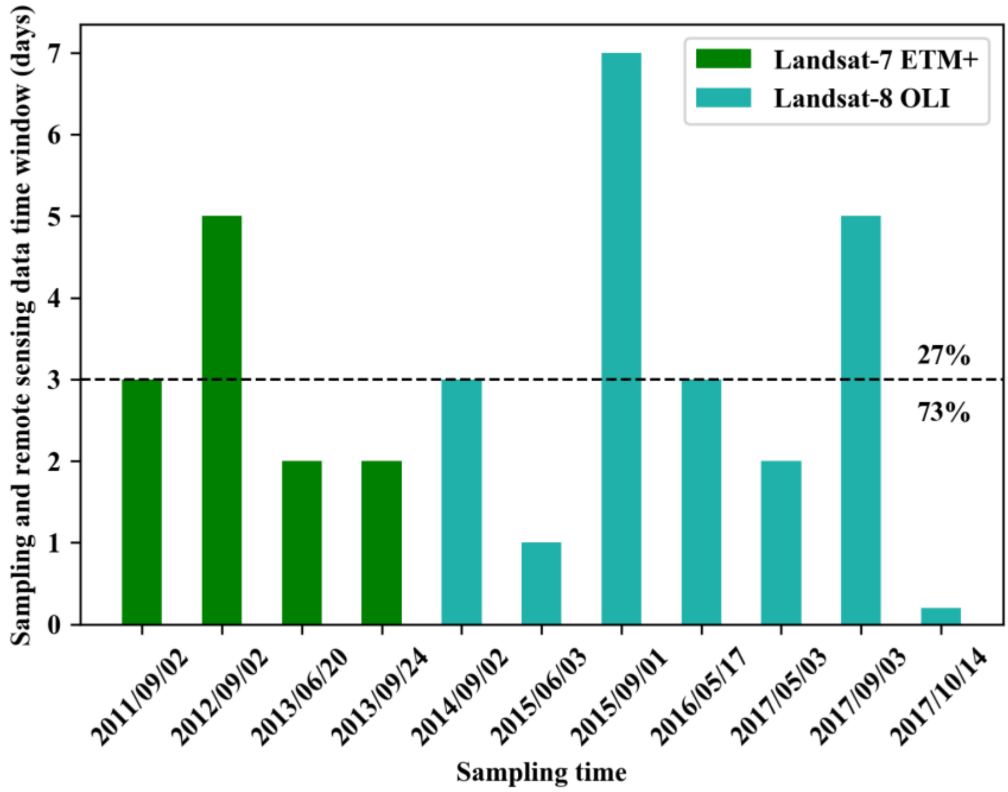

Figure 2. Ebinur Lake's multitemporal Landsat dataset with sampling time window; 73% represents the proportion of time window less than or equal to three days, and 27% represents more than three days, for a total of 42 sample points. (The shortest column indicates that the time window is 0).

Landsat ETM+/OLI and MOD09GA were downloaded from the Geospatial Data Cloud (http://www.gscloud.cn/ (accessed on 15 December 2021)). The fast line-of-sight atmospheric analysis of spectral hypercubes (FLAASH) module of ENVI 5.5 was used for atmospheric correction, adopting the MODTRAN4 radiative transfer model that has been recognized as the best [34]. The Normalized Difference Water Index (NDWI) served as the land mask to obtain the reflectance image of Ebinur Lake [35]. MOD09GA for MODIS rasterized two levels of product data, using the GEE (Google Earth Engine) Cloud Remote Sensing Platform (https://earthengine.google.com/ (accessed on 24 December 2021)) to download. The data were cut according to the study area, filtered by time and band, and reprojected into the UTM-WGS 84 geographical coordinate system with a 30 m resampling. Landsat and sampling time synchronization dates covering the study area are shown in Figure 2. The spatiotemporal fusion data pairs of Landsat and MODIS are shown in Table 2.

Table 2. The spatiotemporal resolution of the Landsat and MODIS data for Ebinur Lake and the corresponding dates.

Landsat 8	Spatiotemporal Resolution	MOD09GA	Spatiotemporal Resolution	Prediction Time
2017-05-08 2017-08-28 2017-10-15	30 m/16 d	2017-05-08 2017-08-29 2017-10-14	500 m/1 d	2017-08-28 (30 m)

The GPS coordinates of sampling points were discretized into space, and the sampling points were overlaid with Landsat 8 images of Ebinur Lake. The reflectance values of B2–B5 (Blue, Green, Red, NIR) bands of Landsat 8 at the sampling points were extracted by ArcGIS. The extracted reflectance values and the observed SPM concentrations were used for inversion model construction and validation.

3. Methods

3.1. ESTARFM Algorithm

The enhanced spatiotemporal fusion algorithm (ESTARFM) was used to generate fused images of Ebinur Lake's surface [24]. The algorithm considers the problem of changing reflectivity over time and is suitable for the changing characteristics of the high SPM in Ebinur Lake. It required the Landsat and MODIS image pairs of two periods of time. The Landsat image was fused by calculation processes shown in Figure 3 [20].

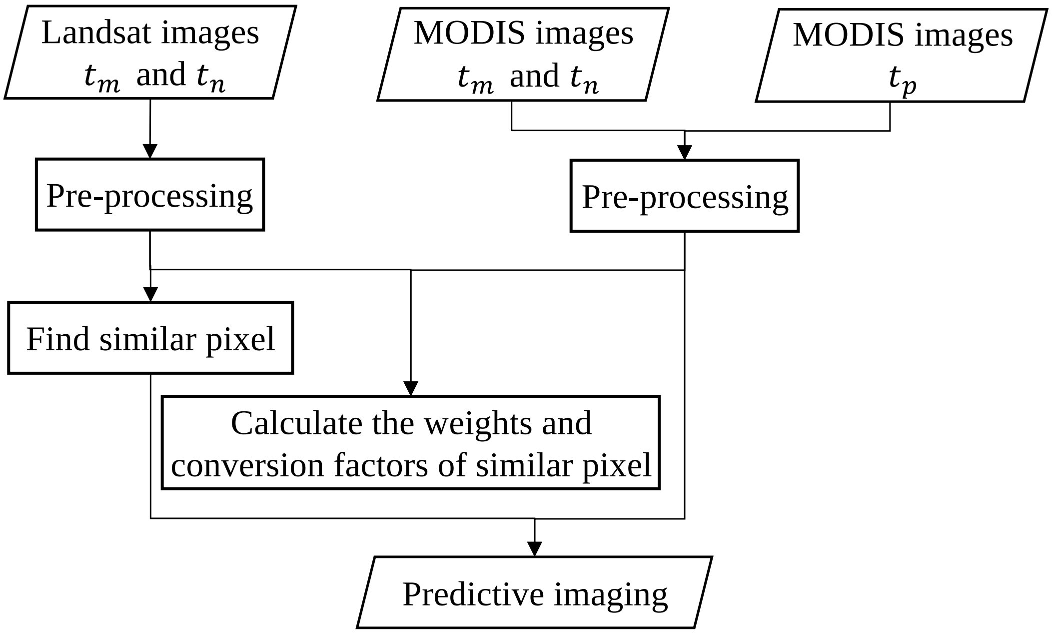

Figure 3. The calculation processes in realizing the ESTARFM model.

The ESTARFM model took into full account the spatial heterogeneity of MODIS (coarse spatial, high temporal resolution images) pixels and introduced conversion factors to improve the fusion simulation results. A moving window of a given size was constructed by taking the simulated pixel as the central pixel. The homogeneous pixel, whose spectral features are similar to the central pixel, was calculated and selected within the moving window to assign weights. Finally, the central value was calculated. The central image element value was expressed by Equation (1) [24]:

$$L_b(x_{\frac{w'}{2}}, y_{\frac{w'}{2}}, T) = L_b(x_{\frac{w'}{2}}, y_{\frac{w'}{2}}, T') + \sum_{i=1}^{n} W_i \times v_i \times \left(M_b(x_i, y_i, T) - M_b\left(x_i, y_i, T'\right)\right) \quad (1)$$

where L_b and M_b are Landsat (fine spatial, low temporal resolution images) and MODIS data in band b; w' is the moving window size; $(x_{w'/2}, y_{w'/2})$ is the simulated image position; T, T' is time; W_i is the weight of the ith image similar to the simulated image spectrum; v_i is the conversion factor of the ith image similar to the simulated image spectrum; n is the number of images similar to the simulated image spectrum; and (x_i, y_i) is the position of the first image similar to the simulated image spectrum.

The Landsat and MODIS data of t_1, t_3 and MODIS data of t_2 were used to simulate the Landsat data of t_2 before and after time and MODIS data of t_2 in the intermediate time: $L_{b,t}(x_{w'/2}, y_{w'/2}, t)$. The simulated t_1, t_3 moment fine data of the t_2 moment were weighted to obtain the more accurate t_2 moment simulated data, and the weight ε_t was calculated as shown in Equation (2). The simulated central pixel value was calculated from Equation (3) to obtain the simulated remote sensing data with a high spatial and temporal resolution for Ebinur Lake [27].

$$\varepsilon_t = \frac{\frac{1}{\left|\sum_{j=1}^{w'}\sum_{i=1}^{w'} M_b\left(X_i,Y_j,t\right)-\sum_{j=1}^{w'}\sum_{i=1}^{w'} M_b\left(X_i,Y_j,t_2\right)\right|}}{\sum_t\left(\frac{1}{\left|\sum_{j=1}^{w'}\sum_{i=1}^{w'} M_b\left(x_i,y_j,t\right)-\sum_{j=1}^{w'}\sum_{i=1}^{w'} M_b\left(x_i,y_j,t_2\right)\right|}\right)}, t = t_1, t_3 \quad (2)$$

$$L_b\left(x_{\frac{w'}{2}}, y_{\frac{w'}{2}}, t_2\right) = \sum_t \varepsilon_t \times L_{b,t}\left(x_{\frac{w'}{2}}, y_{\frac{w'}{2}}, t\right), t = t_1, t_3 \quad (3)$$

3.2. SPM Inversion Algorithm

Based on the literature, several methods were selected to construct the inversion model for SPM. The PLS method assesses the degree of influence of the overall sample on predicted values, thus the combined effect of the individual factors on the prediction can be fully considered [36,37]. The partial least squares (PLS) method is more efficient than the general multiple regression method and has more relaxed sample requirements. PLS is a regression analysis method based on statistical principles. It adopts the idea of high-dimensional projection to seek the best fitting effect of a linear regression model by extracting principal components and projecting observed variables and predictive variables into a new recessive space [38]. The PLS regression model not only contains the advantages of principal component regression, but also has the characteristics of canonical correlation analysis. This can effectively solve the problem of multiple correlations between variables, and can also find the optimal model through the minimum sum of squares algorithm. It is often used for establishing regression models with fewer observation data but more variables [39]. The basic steps of PLS model establishment are as follows [40]:

(1) Standardized data matrix X and Y of dependent variable were processed, and the obtained standardized matrices were expressed as E0 and F0, respectively.
(2) The first pair of components of E0 and F0, t1 and u1, are linear combinations of standardized variables E0 and F0, respectively, and t1 requires maximum correlation to u1; then, the regression equations of E0 and F0 on t1 are obtained, and the residual matrix E1 and F1 of the regression equation can be obtained. E0 is replaced by E1, and F0 is replaced by F1. The second principal component t2 is obtained by the same method, and the nth principal component (n is less than the rank of matrix X) can be obtained.
(3) Convergence is checked to determine the number of principal components extracted.

SVM is a more commonly used method [41]. The implementation principle involves constructing a hyperplane as the optimal classification surface to maximize the isolated edges. Compared with traditional empirical learning algorithms, SVM can better handle dimensional disasters and local minima. RF is a machine-learning technique, a decision tree—based learner to build bagging integration using the random selection principle for decision tree growth [42].

RF is an integrated learning method for regression and classification, which combines the bagging method, the random subspace method, and the decision tree method to improve prediction performance by integrating multiple decision trees to solve the bottleneck problem of overfitting of single decision trees [43–45]. This algorithm incorporates the bootstrap aggregating method to generate subsets, i.e., M training sample sets Dm (m = 1, 2, 3, . . . , n) of the same size as the original sample set are randomly selected from the original sample set D by bootstrap with put-back, and multiple decision trees are constructed accordingly. When splitting each node of the decision tree, a random subspace method is introduced to draw a subset of features uniformly and randomly from all K features, and an optimal split feature is selected from this subset [46]. Finally, using multiple decision trees in parallel, the mean value of the results of multiple decision trees is obtained as the final prediction result, which can be briefly expressed as:

$$\hat{f} = \frac{1}{B}\sum_{b=1}^{B} f_b(x) \quad (4)$$

where $\hat{f}$ denotes the final prediction result; B is the number of decision trees; f_b denotes the regression function; and x denotes the training sample value.

The advantages of random forest include the use of bootstrapping to alleviate the problem of high variance and weaken the correlation between decision trees; to take advantage of the randomness of selecting features by the random subspace method to enhance the model generalization capability; to average the predicted values of multiple decision trees to improve the prediction accuracy; and to achieve accurate classification and prediction of data. The random forest method is simple and efficient, and only needs to adjust the number of trees in the forest (ntree) and the number of features per node (mtry) to generate a reasonable model quickly and effectively. Compared with other machine-learning methods, random forests are highly resistant to overfitting, have a high tolerance for outliers and noise, and have significant advantages in variable ranking, parameter optimization, and variable analysis and interpretation [47].

3.3. SPM Inversion Model Construction

The PLS, SVM, and RF inversion models were constructed using Landsat images. The key features and advantages of the RF inversion model can be highlighted by comparing the model with the traditional PLS or SVM models. In general, the inversion model construction can be divided into three major steps as follows [3,5,9]:

Firstly, the scikit-learn tool in Python was selected to implement the RF algorithm, in which 70% of the sample points were randomly selected as training samples for parameter search and model construction. The remaining 30% of the samples were used for model validation. Compared to machine-learning methods such as PLS and SVM, the RF algorithm is relatively simple in principle and easy to use since it involves only a few parameters.

Secondly, in the scikit-learn's RF library, the algorithm determines three main parameters: n_estimators, max_features, and random_state. The number of decision trees (n_estimators) in bagging framework parameters is obtained by bootstrap resampling. The use of a small number of decision trees can easily lead to underfitting. Therefore, the accuracy of the model is often improved by increasing the number of trees. However, when that number increases to a certain limit, the performance improvement of the model tends to be stable. Too few features may reduce the models' predictive power, whereas too many may reduce its generalization effect and increase the computational effort needed. The random_state parameter is a random seed. When its value remains unchanged, the same result can be obtained when the tree is built with the same training set. However, changing its value will generate different results.

Finally, the parameters of the RF model were set as: random_state at 64, n_estimators optimal result at 12, and max_features at auto. PLS was set according to the default parameters. SVM used a linear kernel function, and other parameters were set by default.

3.4. Evaluation of Spatiotemporal Fusion Image Accuracy

The degrees of superiority and inferiority of the spatiotemporal fusion image and real image quality were evaluated quantitatively. This step was achieved by the Python image processing function library scikit-image tool for accuracy evaluation analysis. ${R_{IF}}^2$, the normalized root mean square error (NRMSE), the peak signal-to-noise ratio (PSNR), and the structural similarity index (*SSIM*) were selected as image quality evaluation indicators [48,49]. We understood the size of the real image I as $m \times n$, F as the spatiotemporal fusion image, $I_{(i,j)}$ as the real image pixel value, and $F_{(i,j)}$ as the spatiotemporal fusion image pixel value.

$R_{IF}{}^2$ evaluated the degree of consistency between spatiotemporal fusion images and real images:

$$R_{IF}{}^2 = \left(\frac{\sum_{i=1}^{m}\sum_{j=1}^{n}\left(I_{(i,j)} - \overline{I}\right)\left(F_{(i,j)} - \overline{F}\right)}{\sqrt{\sum_{i=1}^{m}\sum_{j=1}^{n}\left(I_{(i,j)} - \overline{I}\right)^2}\sqrt{\sum_{i=1}^{m}\sum_{j=1}^{n}\left(F_{(i,j)} - \overline{F}^2\right)}} \right)^2 \tag{5}$$

NRMSE normalized the value of *RMSE* to between (0,1) in order to facilitate the accuracy evaluation of different methods. *RMSE* is the square root of the deviation of the reflectance value of the spatiotemporal fused image and the real image from the square root of the image matrix ratio. The equation is:

$$RMSE = \sqrt{\frac{\sum_{i=1}^{m}\sum_{j=1}^{n}\left(I_{(i,j)} - F_{(i,j)}\right)^2}{mn}} \tag{6}$$

$$NRMSE = \frac{RMSE}{\overline{o}} \tag{7}$$

The peak signal-to-noise ratio (*PSNR*) evaluates the information in the fused image. A larger value means less image information loss. The mean square error (*MSE*) is defined as:

$$MMSE = \frac{1}{mn}\sum_{i=0}^{m-1}\sum_{j=0}^{n-1}[I(i,j) - F(i,j)]^2 \tag{8}$$

$$PSNR = 10 \cdot log_{10}\left(\frac{MAX_{(i,j)}^2}{MSE}\right) \tag{9}$$

where $MAX_{(i,j)}$ is the maximum image element of the image.

The structural similarity index (*SSIM*) evaluated the degree of structural similarity between the spatiotemporal fused images and real images:

$$SSIM = \frac{(2u_I u_F + C_1)(2\sigma_{I \cdot F} + C_2)}{(u_I{}^2 + u_F{}^2 + C_1)(\sigma_I{}^2 + \sigma_F{}^2 + C_2)}) \tag{10}$$

where u_I and u_F represent the mean values, σ_I and σ_F represent the variance between real images and fused images, respectively, and $\sigma_{I \cdot F}$ represents the covariance between these two images. The C_1 and C_2 are the two closest-to-0 constants that are used to stabilize the results. A *SSIM* close to 1 indicates a higher structural similarity between the two scenes.

3.5. Inversion Model Stability and Accuracy Evaluation

The Python statistical function library scipy.stats was used for statistical analysis. Three metrics, namely R^2, *RMSE*, and mean absolute error (*MAE*), tested whether the simulated and real measured values were consistent. The calculation principles of R^2 and *RMSE* have been explained in Section 3.3. *MAE* represents the mean of the absolute value of the deviation between the predicted value and the true value. Recognition-primed decision (*RPD*) characterizes the ratio of standard deviation to *RMSE*, which is an important index to evaluate the model's predictive ability.

Therefore, *MAE* was used as an index to evaluate the reliability of the RF model with two equations [50,51]:

$$MAE = \frac{1}{n}\sum_{i=1}^{n}|y_i - y_i| \tag{11}$$

$$RPD = \frac{SD}{RMSE} \tag{12}$$

In Equation (11), y_i denotes the predicted value and $y_i{}'$ represent the measured value. In Equation (12), *SD* represents the standard deviation, and *RMSE* is the root mean square error. *RPD* > 2 indicates that the model has an excellent predictive ability; if 1.4 < *RPD* < 2, the model offers a rough estimate; if *RPD* < 1.4, the model is extremely poor and cannot make accurate predictions [52,53].

4. Results and Analysis

4.1. Performance Evaluation of the Spatiotemporal Fusion Model

The predicted 30 m spatial resolution image of Ebinur Lake taken on 29 August 2017, was enlisted as a research example. The ESTARFM model was adopted as the main model, while the FSDAF model was used for comparison to verify model accuracy and feasibility. Interactive data language (IDL) was used to implement the algorithm. Landsat 8 and MODIS on 8 May 2017, Landsat 8 on 15 October 2017, and MODIS on 14 October 2017 were first used as the input image pairs for the ESTARFM model. Then, the Landsat 8 image taken on 29 August 2017 was predicted. Secondly, the Landsat 8 and MODIS images of 8 May 2017 were used as the inputs of the FSDAF model, and the MODIS of 29 August 2017 was used to predict the fused FSDAF image of the same date. Finally, the fused ESTARFM and FSDAF images were compared, analyzed, and validated with the Landsat 8 image taken on 29 August 2017.

Figure 4 compares the ESTARFM and FSDAF fusion images with the real Landsat 8 images. The NDWI index extracted the lake surface. The visual interpretation was corrected for the lake coverage to achieve the study's required accuracy. Blue, green, and red true color bands displayed the lake image, which could visually discriminate the spatiotemporal fusion model to better generate predicted date images. The quality of the fused images and the retention of spectral information were quantitatively evaluated by four metrics, namely R^2, NRMSE, PSNR, and *SSIM* (Table 3 and Figure 5). The quality of the ESTARFM fused image was better than that of the FSDAF model. The four evaluation metrics in the green and red bands indicated that the ESTARFM and FSDAF models' fusion image quality was relatively consistent. However, in the blue and NIR bands, the FSDAF model fusion image quality was poorer, with a R^2 of 0.46, NRMSE of 0.59, PSNR of 46.22, and SSIM of 0.45, which were lower than the accuracy of ESTARFM fusion images. Therefore, the ESTARFM model was chosen to fuse the images for the ensuing SPM inversion study.

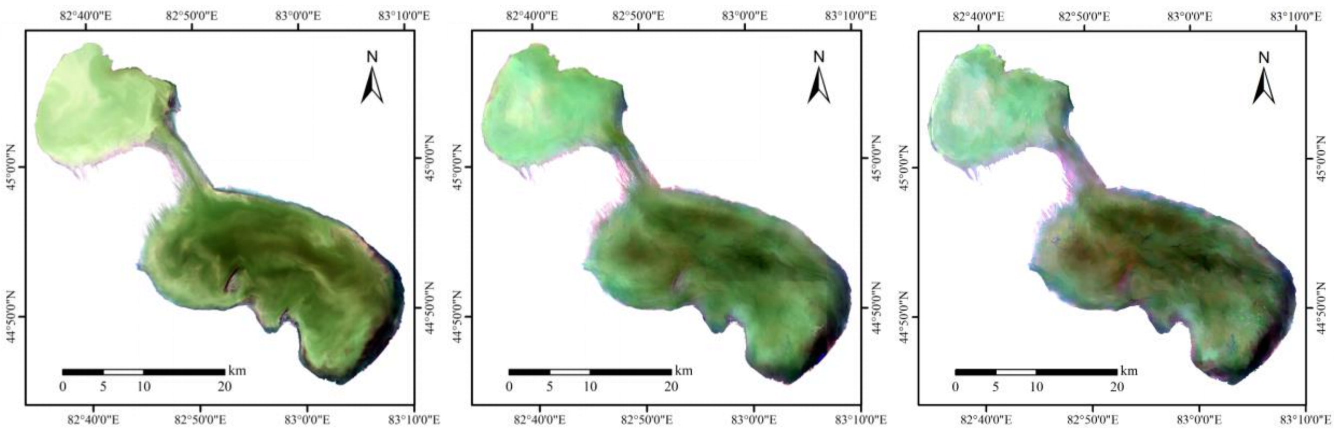

(**a**) (**b**) (**c**)

Figure 4. Comparison of the fusion images of (**a**) Landsat 8; (**b**) ESTARFM; and (**c**) FSDAF.

Table 3. The evaluation of fusion image accuracy for the ESTARFM and FSDAF models.

Band	R^2		NRMSE		PSNR		SSIM	
	ESTARFM	FSDAF	ESTARFM	FSDAF	ESTARFM	FSDAF	ESTARFM	FSDAF
Blue	0.70	0.66	0.13	0.21	48.26	44.02	0.61	0.53
Green	0.82	0.83	0.08	0.08	48.44	48.48	0.70	0.70
Red	0.85	0.85	0.12	0.13	48.22	47.64	0.75	0.71
NIR	0.72	0.46	0.42	0.59	49.23	46.22	0.62	0.45

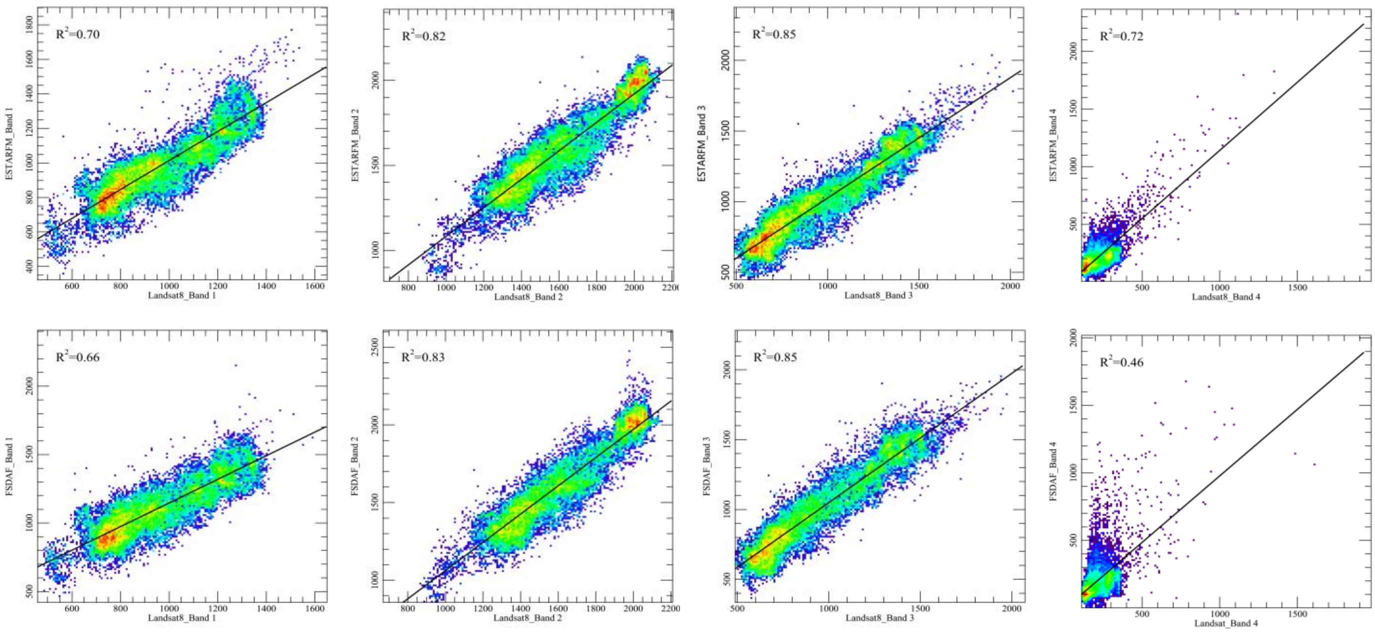

Figure 5. Scatter plots of the coefficient of determination (R^2) for blue, green, red, and NIR bands of the ESTARFM and FSDAF fusion images.

4.2. SPM Inversion Model

4.2.1. Screening of Sensitive Bands

The absorption and scattering characteristics of light radiation by various substances in lake water determine its spectral reflection characteristics. When the SPM content in Ebinur Lake changes, its spectral reflection properties will change correspondingly, leading to correlations between different bands of image and SPM.

The Landsat 8 and MODIS fusion images had poor consistency on B11 and B12 in the short-wave infrared band. This issue could affect the fusion image quality and cause a large error in the inversion of SPM. Thus, more variables were required for the satellite-based SPM measurement, and it was not possible to rely on a single image band such as the NIR band. Instead, multiple bands are required for satellite-based SPM inversion modeling. The reflectance of the B2 to B5 bands of Landsat 8 and the measured value of SPM for Pearson correlation analysis were selected. The sensitive band of SPM was obtained with the aid of correlation analysis following the principle of retaining the maximum amount of information (Figure 6) to ensure the best fitting effect of the RF model.

4.2.2. SPM Inversion Model Performance

Then, the inversion models were trained and built, and their predictive power and model accuracy were evaluated. The analysis in Table 4 shows the inversion models (PLS, SVM, and RF) built on Landsat imagery. The R^2, *RMSE* and *MAE* of the RF inversion model were significantly better than those of PLS and SVM for Landsat images. Moreover, the relative analysis error (*RPD*) of the RF inversion model can be rated as very good.

Considering the accuracy and stability indicators, the RF inversion model offered the best option for predicting the high SPM in Ebinur Lake.

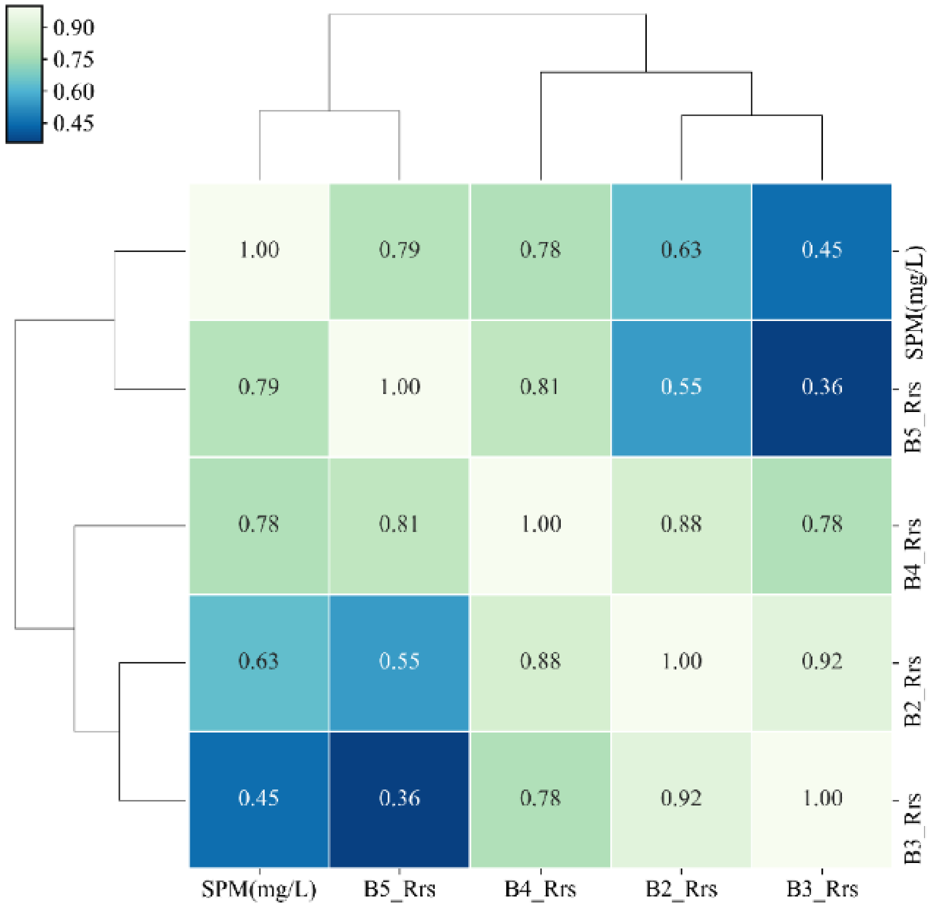

Figure 6. Schematic diagram of the correlations between the sensitive bands of the Landsat 8 B2–B5 reflectance data.

Table 4. Evaluation of the accuracy by PLS, SVM, and RF inversion models.

Remote Sensing Image	Evaluation Indicator	PLS		SVM		RF	
		Training Set	Verification Set	Training Set	Verification Set	Training Set	Verification Set
Landsat 8	R^2	0.79	0.57	0.65	0.50	0.92	0.78
	RMSE	1420.90	2530.50	1873.64	2750.76	870.75	1823.64
	MAE	1175.51	1495.02	1072.62	1448.06	587.39	1026.36
	RPD	1.55		1.41		2.13	

4.3. SPM Inversion Performance of Spatiotemporal Fusion Images

The RF Landsat inversion model was used to analyze the SPM concentrations from Landsat 8 and ESTARFM fusion images taken on 29 August 2017. Figure 7 denotes the SPM distribution in Ebinur Lake, indicating an overall high concentration at an average of 498.73 mg/L for Landsat 8 and 535.98 mg/L for ESTARFM. A sharp SPM increase was induced in the near-shore area with vigorous interactions between wind-agitated lake water and lake-bottom sediments. In the lake's small northern enclave north of the neck (the constricted portion), the lake bottom was affected by a high amount of salinization during the water-scarce season. High salinity causes coagulation or flocculation, which leads to low SPM concentrations during the dry season. In the central neck of the lake, the SPM level was elevated due to the large influx of water from the main southern portion into the northern enclave, creating the scouring effect.

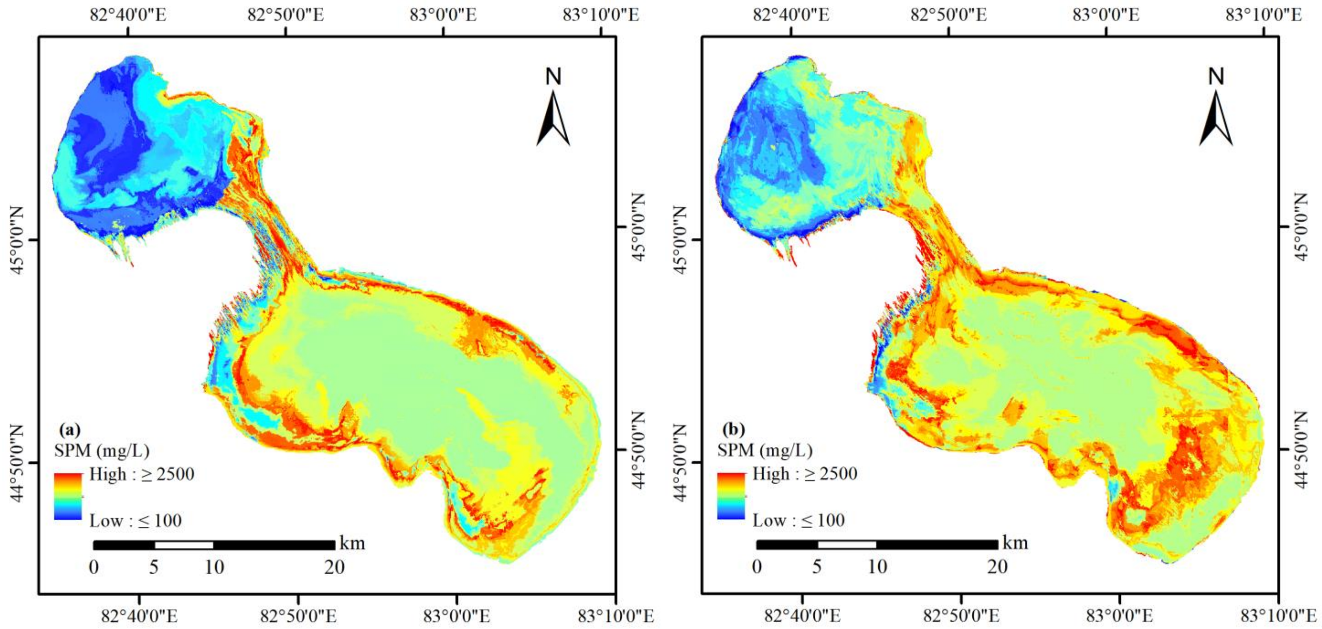

Figure 7. Inversion of SPM concentration distribution from Landsat 8 and ESTARFM fusion images. (**a**) Landsat 8_SPM; (**b**) ESTARFM_SPM.

The spatial distribution of SPM between the Landsat and ESTARFM inversions was similar, as shown in Figure 7. SPM concentrations were mainly constant in the main lake, northern enclave, and lake neck areas. To quantitatively assess the Landsat and ESTARFM inverse SPM concentrations, a validation procedure was conducted using the data measured on 3 September 2017. The results are summarized in Figure 8, which shows that the Landsat inverse SPM (Landsat 8_SPM) strongly correlated (R = 0.88) with the measured SPM. The ESTARFM inverse SPM (ESTARFM_SPM) correlated with the measured SPM at R = 0.88, and Landsat8_SPM with ESTARFM_SPM at R = 0.96.

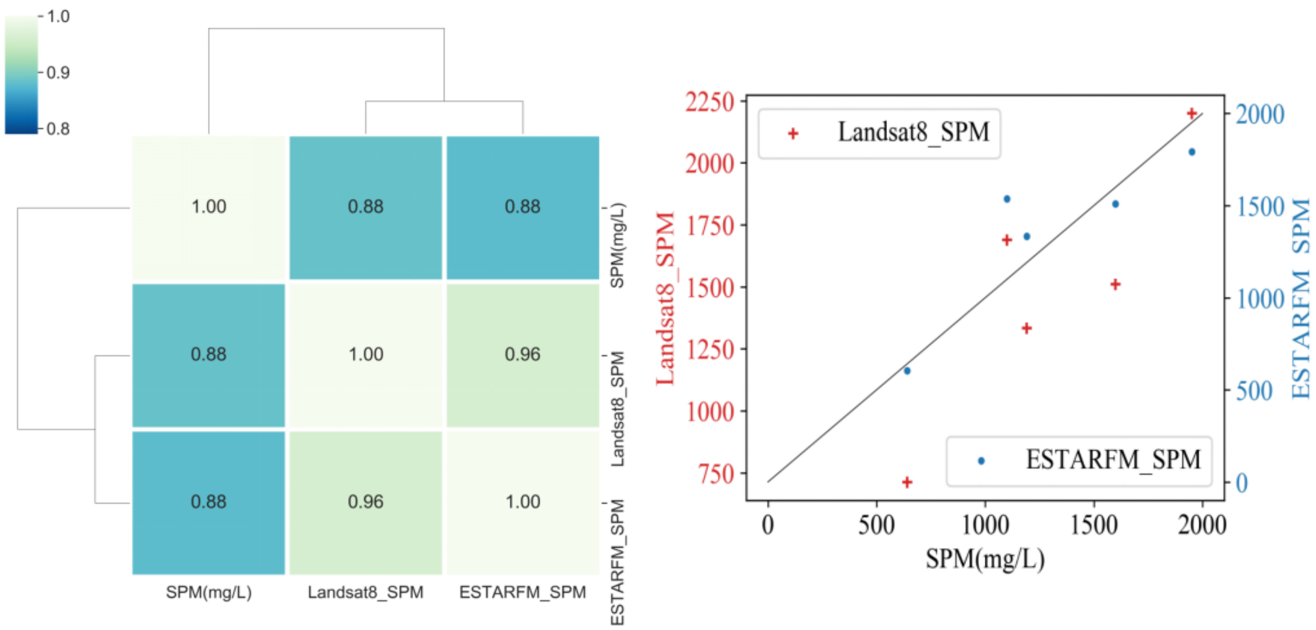

Figure 8. The correlations between Landsat 8 and ESTARFM inversions of SPM and measured SPM concentrations.

A total of 1000 random points were selected from the Landsat SPM inversion map and the ESTARFM fused image inversion map to measure the reliability of ESTARFM fused image inversion of SPM concentrations. Point determination followed the principle of using the minimum allowable distance (30 m) when using the random points creation tool in ArcGIS. Figure 9 indicates that the correlation between the two reached R = 0.65 with $p < 0.01$ significance level. This result further illustrates the accuracy and feasibility of ESTARFM fusion image inversion of SPM.

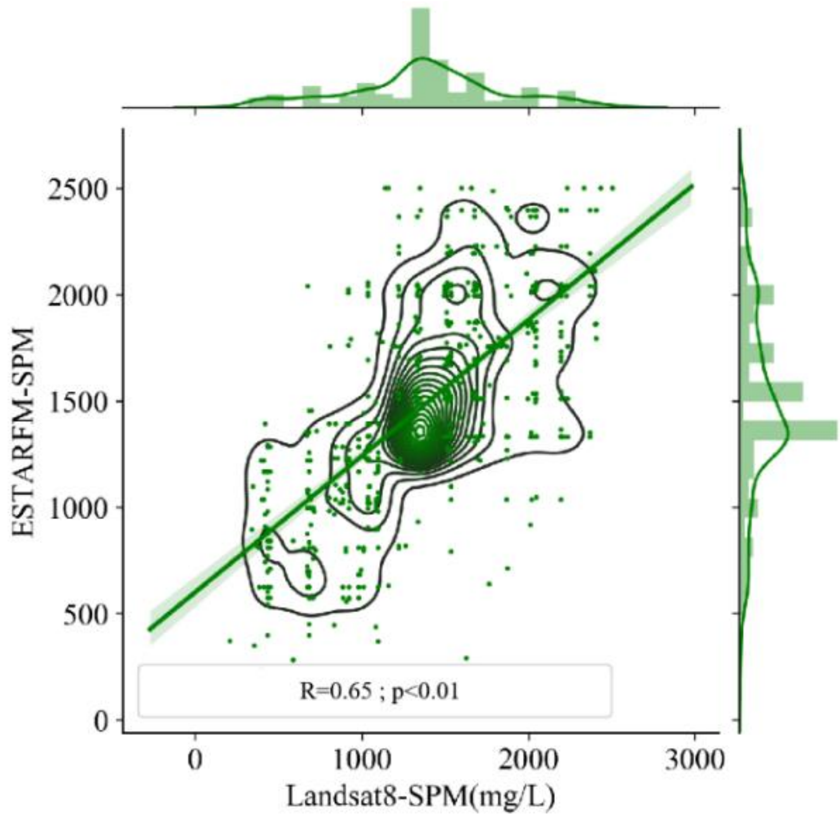

Figure 9. The correlation between Landsat 8 and ESTARFM inversions of SPM concentrations.

5. Discussion

Currently, spatiotemporal fusion models have been applied to mainly terrestrial features with strong spectral reflection information, such as land use cover, vegetation, and soil [54]. However, few studies focus on water bodies. The relevant cases include the use of spatiotemporal fusion models to study water level changes, such as chlorophyll-a (Chl-a) and chemical oxygen demand (COD), in freshwater lakes [55]. The inversion study of SPM in Shenzhen Sea using a spatiotemporal fusion model has achieved good results [33]. However, the above studies were conducted on freshwater lakes and coastal regions [56]. There is a lack of relevant studies on brackish lakes in inland drylands. Therefore, this paper applied a spatiotemporal fusion model to assess the high and variable SPM in Ebinur Lake. After comparing and analyzing the FSDAF and ESTARFM models, the former, which has more accurate results, was adopted. The feasibility of applying this spatiotemporal fusion model to the inversion of SPM in water bodies was further verified by a time series MODIS SPM inversion experiment for Ebinur Lake. A large accuracy difference was found between the fused visible band and the NIR, which is most likely due to the absorption of NIR by water, resulting in a weaker signal and low fusion accuracy. In the future, SPM concentration inversion followed by fusion research can be considered, which will improve the accuracy.

The most common SPM inversion models in the literature are regression models; however, because our work exclusively focuses on specific linear relationships, these models are less appropriate [57,58]. The accuracy of PLS is lower than that of RF models. Other techniques, such as SVM and artificial neural network models, cannot mechanically elaborate the complex internal structure of the model and suffer from various limitations, such as overfitting and computational overload [59]. Therefore, we considered alternative schemes and found that RF models have relative advantages in terms of flexibility, robustness, parameter optimization, and explanatory analysis [60]. The findings show that the correlation coefficient and model prediction accuracy of RF for SPM are significantly better than PLS and SVM. This model applies to remote sensing monitoring of SPM in Ebinur Lake and similar brackish lakes in inland arid regions, but we still need to collect sample points from other lakes to validate the model. We also need to compare these results with freshwater lakes to highlight the similarities and differences between them.

In this research, a spatiotemporal fusion algorithm is used to generate remote sensing images of a lake's surface for the inversion of the target water quality parameters. The quality and temporal differences of the input image pairs require different computational methods to build the spatiotemporal fusion model [61]. The overall trend of the ESTARFM fused SPM concentration map and the SPM concentration map of Landsat 8 inversion are consistent in performance, but there are still significant differences in the details, e.g., (1) the differences in the shooting time of the MODIS images involved in the fusion; (2) the imperfections of the fusion algorithm itself; and (3) the accuracy of the inversion model, which needs to be further improved. These differences may be caused by a variety of reasons, indicating that for spatiotemporal fusion in water bodies, a momentarily changing object, there is still a certain degree of difficulty, and time and space requirements are very high [62]. We also found that the accuracy of the fused SPM concentration map was lower than that of the original SPM concentration map when we performed accuracy validation [63]. However, the validation sample points are evenly distributed in the 1:1 line, indicating that it is possible to further improve the accuracy in future studies [64]. Using the optimal inversion algorithm combined with the spatiotemporal fusion model, the inversion study of water quality parameters with high spatiotemporal resolution is very promising.

6. Conclusions

This research aims to develop an advanced spatiotemporal fusion model of SPM for an intermontane lake. In general, the study extracted SPM information from Landsat images for the period of 2011–2017. After careful analysis, the RF inversion model was chosen to retrieve the SPM concentrations in Ebinur Lake. The conclusions are as follows:

(1) The overall results of the blue, green, red, and NIR bands generated by ESTARFM were better than FSDAF when compared with the real images.
(2) The RF inversion models based on Landsat images were proven to be better than PLS and SVM.
(3) The visual perspective and accuracy assessment showed some consistency in the SPM concentration retrieved from the fused images of Landsat 8 and ESTARFM.

In the future, we will select analytical or semi-analytical and other algorithms combined with the improved spatiotemporal fusion model for inversion studies of water quality parameters that require high spatiotemporal resolution. We believe this will achieve better accuracy.

Author Contributions: Conceptualization, F.Z.; methodology, F.Z. and P.D.; software, P.D.; validation, F.Z. and P.D.; formal analysis, F.Z.; investigation, W.W.; resources, F.Z. and C.L.; data curation, F.Z., P.D., C.L. and W.W.; writing—original draft preparation, F.Z. and P.D.; writing—review and editing, F.Z., P.D., C.Y.J., V.C.J., N.W.C., M.L.T. and H.-T.K.; visualization, P.D. and J.S.; supervision, F.Z.; project administration, F.Z.; funding acquisition, F.Z. All authors have read and agreed to the published version of the manuscript.

Funding: This research was funded by the National Natural Science Foundation of China (Grant Number 42261006), the State Key Laboratory of Lake Science and Environment (Grant Number 2022SKL007), and the Tianshan Talent Project (Phase III) of the Xinjiang Uygur Autonomous Region.

Data Availability Statement: The data presented in this study are available on request from the corresponding author. The data are not publicly available due to confidentiality.

Acknowledgments: We appreciate the helpful comments offered by the anonymous reviewers and editors to improve our manuscript.

Conflicts of Interest: The authors declare no conflict of interest.

References

1. Xu, Z.Q.; Shen, J.; Qu, Y.Q.; Chen, H.F.; Zhou, X.L.; Hong, H.C.; Sun, H.J.; Lin, H.J.; Deng, W.J.; Wu, F.Y. Using simple and easy water quality parameters to predict trihalomethane occurrence in tap water. *Chemosphere* **2022**, *286*, 131586. [CrossRef]
2. Wang, J.; Sheng, Y.; Tong, T. Monitoring decadal lake dynamics across the Yangtze Basin downstream of Three Gorges Dam. *Remote Sens. Environ.* **2014**, *152*, 251–269. [CrossRef]
3. Hou, X.; Feng, L.; Duan, H.; Chen, X.; Sun, D.; Shi, K. Fifteen-year monitoring of the turbidity dynamics in large lakes and reservoirs in the middle and lower basin of the Yangtze River, China. *Remote Sens. Environ.* **2017**, *190*, 107–121. [CrossRef]
4. Zhu, S.D.; Zhang, F.; Zhang, Z.Y.; Kung, H.; Yushanjiang, A. Hydrogen and Oxygen Isotope Composition and Water Quality Evaluation for Different Water Bodies in the Ebinur Lake Watershed, Northwestern China. *Water* **2019**, *11*, 2067. [CrossRef]
5. Sagan, V.; Peterson, K.T.; Maimaitijiang, M.; Sidike, P.; Sloan, J.; Greeling, B.A.; Maalouf, S.; Adams, C. Monitoring inland water quality using remote sensing: Potential and limitations of spectral indices, bio-optical simulations, machine learning, and cloud computing. *Earth-Sci. Rev.* **2020**, *205*, 103187. [CrossRef]
6. Sun, Z.; Li, J.; Tian, L.; Cehn, B.; Hu, X. Spatial Variation and Risk Assessment of Arsenic and Heavy Metals in Surface Water and Suspended Particulate Matter in Tail Reaches of the Yellow River, China. *Chin. Geogr. Sci.* **2021**, *31*, 181–196. [CrossRef]
7. Cao, Q.; Yu, G.; Qiao, Z. Application and recent progress of inland water monitoring using remote sensing techniques. *Environ. Monit. Assess.* **2023**, *195*, 1–16. [CrossRef]
8. Ho, C.R.; Liu, A.K. Preface: Remote Sensing Applications in Ocean Observation. *Remote Sens.* **2023**, *15*, 415. [CrossRef]
9. Chen, J.; Chen, S.; Fu, R.; Li, D.; Jiang, H.; Wang, C.; Peng, Y.; Jia, K.; Hicks, B.J. Remote sensing big data for water environment monitoring: Current status, challenges, and future prospects. *Earth's Future* **2022**, *10*, e2021EF002289. [CrossRef]
10. Lv, H.; Jiang, N.; Li, X.G. The Study on Water Quality of in Land Lake Monitoring by Remote Sensing. *Adv. Earth Sci.* **2005**, *20*, 185–192.
11. Chen, C.; Mao, Z.H.; Tang, F.P.; Han, G.Q.; Jiang, Y.Z. Declining riverine sediment input impact on spring phytoplankton bloom off the Yangtze River Estuary from 17-year satellite observation. *Cont. Shelf Res.* **2017**, *135*, 86–91. [CrossRef]
12. Lee, Z.; Carder, K.L.; Arnone, R.A. Deriving inherent optical properties from water color: A multiband quasi-analytical algorithm for optically deep waters. *Appl. Opt.* **2002**, *41*, 5755–5772. [CrossRef]
13. Rotta, L.; Alcântara, E.; Park, E.; Bernardo, N.; Watanabe, F. A single semi-analytical algorithm to retrieve chlorophyll-a concentration in oligo-to-hypereutrophic waters of a tropical reservoir cascade. *Ecol. Indic.* **2021**, *120*, 106913. [CrossRef]
14. Lu, H.F.; Ma, X. Hybrid decision tree-based machine learning models for short-term water quality prediction. *Chemosphere* **2020**, *249*, 126169. [CrossRef]
15. Sun, J.; Zhong, G.; Huang, K.; Dong, J. Banzhaf random forests: Cooperative game theory based random forests with consistency. *Neural Netw.* **2018**, *106*, 20–29. [CrossRef]
16. Grimm, R.; Behrens, T.; Märker, M.; Elsenbeer, H. Soil organic carbon concentrations and stocks on Barro Colorado Island-Digital soil mapping using Random Forests analysis. *Geoderma* **2008**, *146*, 102–113. [CrossRef]
17. Su, Z.H.; Chen, L.; Ma, R.H.; Luo, J.H.; Liang, Q.O. Effect of land use change on lake water quality in different buffer zones. *Appl. Ecol. Environ. Res.* **2015**, *13*, 639–653.
18. Dube, T.; Shekede, M.D.; Massari, C. Remote sensing for water resources and environmental management. *Remote Sens.* **2023**, *15*, 18. [CrossRef]
19. Huang, Z.; Li, Y.; Bai, M.; Wei, Q.; Gu, Q.; Mou, Z.; Zhang, L.; Lei, D. A Multiscale Spatiotemporal Fusion Network Based on an Attention Mechanism. *Remote Sens.* **2023**, *15*, 182. [CrossRef]
20. Zhu, X.; Cai, F.; Tian, J.; Williams, T.K.A. Spatiotemporal fusion of multisource remote sensing data: Literature survey, taxonomy, principles, applications, and future directions. *Remote Sens.* **2018**, *10*, 527. [CrossRef]
21. Liang, Z.H. *Research on the Construction of Tasseled Cap Transform Indices Time Series Data Sets Based on Spatial-Temporal Fusion Algorithm*; Lanzhou University: Lanzhou, China, 2015. (In Chinese)
22. Sun, L.; Gao, F.; Xie, D.; Anderson, M.; Chen, R.; Yang, Y.; Yang, Y.; Chen, Z. Reconstructing daily 30m NDVI over complex agricultural landscapes using a crop reference curve approach. *Remote Sens. Environ.* **2020**, *253*, 112156. [CrossRef]
23. Gao, F.; Masek, J.; Schwaller, M.; Hall, F. On the blending of the Landsat and MODIS surface reflectance: Predicting daily Landsat surface reflectance. *IEEE Trans. Geosci. Remote Sens.* **2006**, *44*, 2207–2218.

24. Zhu, X.; Chen, J.; Gao, F.; Chen, X.; Masek, J.G. An enhanced spatial and temporal adaptive reflectance fusion model for complex heterogeneous regions. *Remote Sens. Environ.* **2010**, *114*, 2610–2623. [CrossRef]
25. Cheng, Q.; Liu, H.; Shen, H.; Wu, P.; Zhang, L. A Spatial and Temporal Nonlocal Filter-Based Data Fusion Method. *IEEE Trans. Geosci. Remote Sens.* **2017**, *55*, 4476–4488. [CrossRef]
26. Xie, D.; Zhang, J.; Zhu, X.; Pan, Y.; Liu, H.; Yuan, Z.; Yun, Y. An improved STARFM with help of an unmixing-based method to generate high spatial and temporal resolution remote sensing data in complex heterogeneous regions. *Sensors* **2016**, *16*, 207. [CrossRef]
27. Zhu, X.; Helmer, E.H.; Gao, F.; Liu, D.; Chen, J.; Lefsky, M.A. A flexible spatiotemporal method for fusing satellite images with different resolutions. *Remote Sens. Environ.* **2016**, *172*, 165–177. [CrossRef]
28. Huang, B.; Song, H. Spatiotemporal Reflectance Fusion via Sparse Representation. *IEEE Trans. Geosci. Remote Sens.* **2012**, *50*, 3707–3716. [CrossRef]
29. Wang, L.; Li, Y.; Wang, Y.; Guo, J.; Xia, Q.; Tu, Y.; Nie, P. Compensation benefits allocation and stability evaluation of cascade hydropower stations based on Variation Coefficient -Shapley Value Method. *J. Hydrol.* **2021**, *599*, 126277. [CrossRef]
30. Li, P.; Ke, Y.; Wang, D.; Ji, H.; Chen, S.; Chen, M.; Lyu, M.; Zhou, D. Human impact on suspended particulate matter in the Yellow River Estuary, China: Evidence from remote sensing data fusion using an improved spatiotemporal fusion method. *Sci. Total Environ.* **2021**, *750*, 141612. [CrossRef]
31. Liu, C.J.; Duan, P.; Zhang, F.; Jim, C.Y.; Tan, M.L.; Chan, N.W. Feasibility of the Spatiotemporal Fusion Model in Monitoring Ebinur Lake's Suspended Particulate Matter under the Missing-Data Scenario. *Remote Sens.* **2021**, *13*, 3952. [CrossRef]
32. *GB11901-89*; Water Quality Determination of Suspended Substance-Gravimetric Method. Peoples' Republic of China: Beijing, China, 1989.
33. Cao, Z.; Duan, H.; Song, Q.; Shen, M.; Ma, R.; Liu, D. Evaluation of the sensitivity of China's next-generation ocean satellite sensor MWI onboard the Tiangong-2 space lab over inland waters. *Int. J. Appl. Earth Obs. Geoinf.* **2018**, *71*, 109–120. [CrossRef]
34. Manoj, K.M.; Bimal, B. 4-Atmospheric parameter retrieval and correction using hyperspectral data. *Hyperspectral Remote Sens.* **2020**, 67–84. [CrossRef]
35. Watson, C.S.; King, O.; Miles, E.S.; Quincey, D.J. Optimising NDWI supraglacial pond classification on Himalayan debris-covered glaciers. *Remote Sens. Environ.* **2018**, *217*, 414–425. [CrossRef]
36. Wold, S.; Ruhe, A.; Wold, H.; Dunn, W.J., III. The Collinearity Problem in Linear Regression. The Partial Least Squares (PLS) Approach to Generalized Inverse. *SLAM J. Sci. Stat. Comput.* **1984**, *5*, 735–743. [CrossRef]
37. Rosipal, R.; Kramer, N. Overview and Recent Advances in Partial Least Squares. In *Subspace, Latent Structure and Feature Selection, Bohinj, Slovenia, 23–25 February 2005*; Springer: Berlin/Heidelberg, Germany, 2006; pp. 34–51.
38. Wold, S.; Sjöström, M.; Eriksson, L. PLS-regression: A basic tool of chemometrics. *Chemom. Intell. Lab. Syst.* **2001**, *58*, 109–130. [CrossRef]
39. Huang, W. *Diagnosis and Solution of Collinearity in Multiple Regression Modeling*; Harbin Institute of Technology: Harbin, China, 2012. (In Chinese)
40. Chen, J.H.; Yu, H.L.; Jiang, D.P.; Zhang, Y.Z.; Wang, K.Q. A novel NIRS modelling method with OPLS-SPA and MIX-PLS for timber evaluation. *J. For. Res.* **2022**, *33*, 369–376. [CrossRef]
41. Joachims, T. Making Large-Scale SVM Learning Practical. *Tech. Rep.* **1988**, *8*, 499–526.
42. Breiman, L. Random forests. *Mach. Learn.* **2001**, *45*, 5–32. [CrossRef]
43. Breiman, L. Bagging predictors. *Mach. Learn.* **1996**, *24*, 123–140. [CrossRef]
44. Sun, J.Y.; Wang, G.Z.; He, G.J.; Pu, D.C.; Jiang, W.; Li, T.T.; Niu, X.F. Study on the water body extraction using GF-1 data based on adaboost integrated learning algorithm. *Int. Arch. Photogramm. Remote Sens. Spat. Inf. Sci.* **2020**, *42*, 641–648. [CrossRef]
45. Ho, T.K. The random subspace method for constructing decision forests. *IEEE Trans. Pattern Anal. Mach. Intell.* **1998**, *20*, 832–844.
46. Wang, Y.S.; Xia, S.T. A survey of random forests algorithms. *Inf. Commun. Technol.* **2018**, *12*, 49–55.
47. Fang, X.; Wen, Z.; Chen, J.; Wu, S.; Huang, Y.; Ma, M. Remote sensing estimation of suspended sediment concentration based on Random Forest Regression Model. *J. Remote Sens.* **2019**, *23*, 756–772.
48. Wang, Z. Image Quality Assessment: From Error Visibility to Structural Similarity. *IEEE Trans. Image Process.* **2004**, *13*, 600–612. [CrossRef]
49. Horé, A.; Ziou, D. Image quality metrics: PSNR vs. SSIM. In Proceedings of the 2010 20th International Conference on Pattern Recognition, Istanbul, Turkey, 23–26 August 2010; pp. 2366–2369. [CrossRef]
50. Klein, G.A. A recognition-primed decision (RPD) model of rapid decision making. *Decis. Mak. Action Model. Methods* **1993**, *5*, 138–147.
51. Chang, C.W.; Laird, D.A.; Mausbach, M.J.; Hurburgh, C.R. Near-Infrared Reflectance Spectroscopy-Principal Components Regression Analyses of Soil Properties. *Soil Sci. Soc. Am. J.* **2001**, *65*, 480–490. [CrossRef]
52. Yuan, J.; Wang, X.; Yan, C.X.; Wang, S.R.; Ju, X.P.; Li, Y. Soil Moisture Retrieval Model for Remote Sensing Using Reflected Hyperspectral Information. *Remote Sens.* **2019**, *11*, 366. [CrossRef]
53. Amin, I.; Fikrat, F.; Mammadov, E.; Babayev, M. Soil organic carbon prediction by Vis-NIR Spectroscopy: Case Study the Kur-Aras Plain, Azerbaijan. *Commun. Soil Sci. Plant Anal.* **2020**, *51*, 1–9. [CrossRef]
54. Fu, D.; Chen, B.; Wang, J.; Zhu, X.; Hilker, T. An improved image fusion approach based on enhanced spatial and temporal the adaptive reflectance fusion model. *Remote Sens.* **2013**, *5*, 6346–6360. [CrossRef]

55. Zhang, X.C.; Wang, J. The Analysis of Eco-hydrological Structure of Shengjin Lake Wetland based on Spatial and Temporal Fusion Technology of Remote Sensing. *Remote Sens. Technol. Appl.* **2020**, *35*, 1109–1117.
56. Doña, C.; Chang, N.B.; Caselles, V.; Sánchez, J.M.; Camacho, A.; Delegido, J.; Vannah, B.W. Integrated satellite data fusion and mining for monitoring lake water quality status of the Albufera de Valencia in Spain. *J. Environ. Manag.* **2015**, *151*, 416–426. [CrossRef]
57. Carpenter, D.J.; Carpenter, S.M. Modeling inland water quality using Landsat data. *Remote Sens. Environ.* **1983**, *13*, 345–352. [CrossRef]
58. Dörnhöfer, K.; Oppelt, N. Remote sensing for lake research and monitoring-Recent advances. *Ecol. Indic.* **2016**, *64*, 105–122. [CrossRef]
59. Shen, C. A transdisciplinary review of deep learning research and its relevance for water resources scientists. *Water Resour. Res.* **2018**, *54*, 8558–8593. [CrossRef]
60. Shah, S.H.; Angel, Y.; Houborg, R.; Ali, S.; McCabe, M.F. A random forest machine learning approach for the retrieval of leaf chlorophyll content in wheat. *Remote Sens.* **2019**, *11*, 920. [CrossRef]
61. Guan, Q.H.; Ding, M.J.; Zhang, H.; Wang, P. Analysis of applicability about ESTARFM in the middle-lower Yangtze Plain. *J. Geo-Inf. Sci.* **2021**, *23*, 1118–1130.
62. Yang, H.; Du, Y.; Zhao, H.; Chen, F. Water quality Chl-a inversion based on spatio-temporal fusion and convolutional neural network. *Remote Sens.* **2022**, *14*, 1267. [CrossRef]
63. Nazirova, K.; Alferyeva, Y.; Lavrova, O.; Shur, Y.; Soloviev, D.; Bocharova, T.; Strochkov, A. Comparison of in situ and remote-sensing methods to determine turbidity and concentration of suspended matter in the estuary zone of the mzymta river, black sea. *Remote Sens.* **2021**, *13*, 143. [CrossRef]
64. Kim, Y.W.; Kim, T.; Shin, J.; Lee, D.S.; Park, Y.S.; Kim, Y.; Cha, Y. Validity evaluation of a machine-learning model for chlorophyll a retrieval using Sentinel-2 from inland and coastal waters. *Ecol. Indic.* **2022**, *137*, 108737. [CrossRef]